Joule

Article

Accelerated discovery of CO_2-to-C_3-hydrocarbon electrocatalysts with human-in-the-loop

Graphical abstract

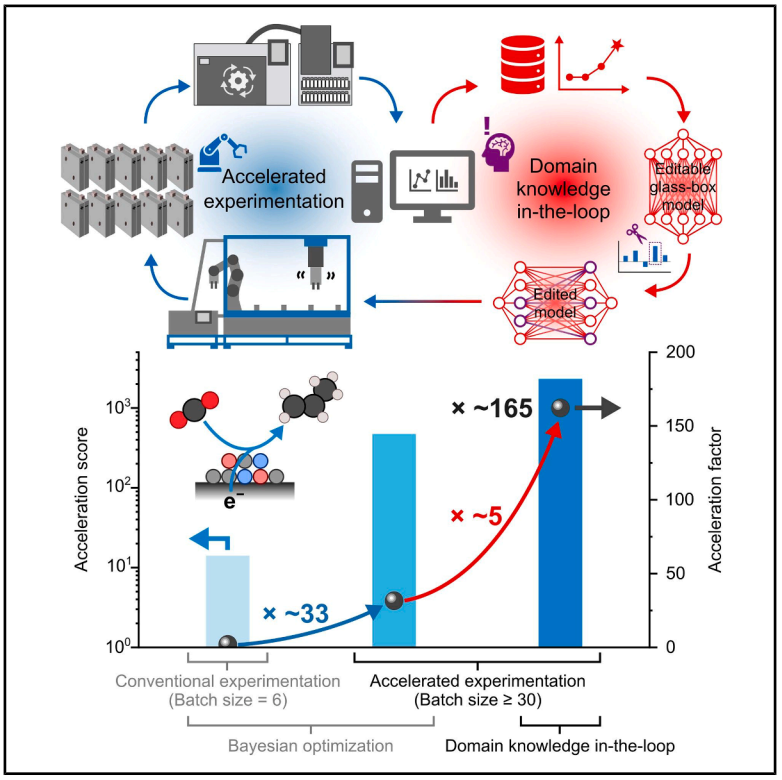

Highlights

- Automated experimentation with ML and expert input accelerates catalyst discovery
- Data mining of 300 catalysts reveals two CO_2-to-C_3 hydrocarbon formation pathways
- Discovered catalyst achieves propylene production rate of 42 mmol g_{cat}^{-1} h^{-1}

Authors

Jiheon Kim, Suhas Mahesh, Hyeon Seok Lee, ..., Jason Hattrick-Simpers, Edward H. Sargent, David Sinton

Correspondence

jason.hattrick.simpers@utoronto.ca (J.H.-S.), ted.sargent@northwestern.edu (E.H.S.), dave.sinton@utoronto.ca (D.S.)

In brief

Despite advances in automation and AI, accelerating discovery in heterogeneous electrocatalysts remains hindered by the experimental challenges of building integrated platforms for synthesis and evaluation, as well as limited performance-relevant data. This work integrates accelerated experimentation, machine learning, and domain expertise to efficiently explore CO_2-to-C_3 electrocatalysts, adding new mechanistic and data-driven insights to energy science.

Kim et al., 2025, Joule 9, 102213
December 17, 2025
https://doi.org/10.1016/j.joule.2025.102213

CellPress

Please cite this article in press as: Kim et al., Accelerated discovery of CO_2-to-C_3-hydrocarbon electrocatalysts with human-in-the-loop, Joule (2025), https://doi.org/10.1016/j.joule.2025.102213

Joule

CellPress

Article

Accelerated discovery of CO_2-to-C_3-hydrocarbon electrocatalysts with human-in-the-loop

Jiheon Kim,[1,2,3,10] Suhas Mahesh,[4,5,10] Hyeon Seok Lee,[2,3] Roham Dorakhan,[1] Yang Bai,[5] Muhammad Imran,[1] Kangming Li,[5] Yutong Liu,[4] Dongha Kim,[2] Sungjin Park,[1] Ali Shayesteh Zeraati,[5] Hyun Sik Moon,[1,2] Xiaodong Li,[2,5] Fatemeh Arabyarmohammadi,[2] Jehad Abed,[6] Brook Wander,[7] Chengqian Wu,[2] Shijie Liu,[2] Yurou Celine Xiao,[2] Rui Kai Miao,[2] Sjoerd Hoogland,[1,3] Jason Hattrick-Simpers,[3,4,5,*] Edward H. Sargent,[1,3,8,9,*] and David Sinton[2,3,5,11,*]

[1]Department of Electrical and Computer Engineering, University of Toronto, Toronto, ON, Canada
[2]Department of Mechanical and Industrial Engineering, University of Toronto, Toronto, ON, Canada
[3]The Alliance for AI-Accelerated Materials Discovery (A3MD), Toronto, ON, Canada
[4]Department of Materials Science and Engineering, University of Toronto, Toronto, ON, Canada
[5]Acceleration Consortium, University of Toronto, Toronto, ON, Canada
[6]Fundamental AI Research, Meta AI, Menlo Park, CA, USA
[7]Department of Chemical Engineering, Carnegie Mellon University, Pittsburgh, PA, USA
[8]Department of Chemistry, Northwestern University, Evanston, IL, USA
[9]Department of Electrical and Computer Engineering, Northwestern University, Evanston, IL, USA
[10]These authors contributed equally
[11]Lead contact
*Correspondence: jason.hattrick.simpers@utoronto.ca (J.H.-S.), ted.sargent@northwestern.edu (E.H.S.), dave.sinton@utoronto.ca (D.S.)
https://doi.org/10.1016/j.joule.2025.102213

CONTEXT & SCALE Recent advances in automation and artificial intelligence have accelerated materials discovery, yet their implementation in heterogeneous electrocatalysts remains limited by challenges in integrating synthesis and performance evaluation, resulting in a lack of practically relevant data. This work establishes a human-in-the-loop accelerated discovery framework that couples robotic experimentation with interpretable machine learning, enabling human experts to refine model predictions during the search. The framework achieves a ~165× acceleration in catalyst discovery, with ~33× derived from accelerated experimentation and ~5× from expert intervention. Applied to a 15-element compositional space, this framework enables the identification of $Cu_{0.98}In_{0.02}$ as a highly active CO_2-to-C_3-hydrocarbon electrocatalyst, achieving a propylene production rate of 42 mmol g_{cat}^{-1} h^{-1} under neutral membrane electrode assembly (MEA) conditions. Analysis of 300 compositions further uncovers two mechanistic pathways—*CO dimerization and *CH_x-mediated coupling—demonstrating that merging automation, human domain expertise, and data-driven analysis can both accelerate discovery and reveal insights into complex catalytic systems.

SUMMARY

Automated high-throughput experimentation combined with artificial intelligence holds the potential to accelerate materials discovery; however, utilizing this approach in heterogeneous electrocatalytic materials has been challenging. Here, we pursue the discovery of multi-element CO_2 electrocatalysts by employing a machine learning algorithm that integrates human domain knowledge to enable on-the-fly editing of feature contributions. By combining this approach with an accelerated experimental platform, we navigate a 15-element space for CO_2-to-C_3 hydrocarbon electrosynthesis and achieve a ~165× acceleration compared with a conventional screening approach—of which ~33× comes from the new experimentation platform and a further ~5× from incorporating human domain knowledge. We identify $Cu_{0.98}In_{0.02}$ as an effective catalyst for propylene electrosynthesis, achieving a production rate of 42 mmol g_{cat}^{-1} h^{-1} in a 25 cm^2 electrolyzer. Data mining on the 300-composition dataset reveals two distinct C–C coupling pathways toward C_3 hydrocarbons—*CO dimerization and *CH_x-mediated coupling—with composition-dependent factors governing each pathway.

Please cite this article in press as: Kim et al., Accelerated discovery of CO_2-to-C_3-hydrocarbon electrocatalysts with human-in-the-loop, Joule (2025), https://doi.org/10.1016/j.joule.2025.102213

INTRODUCTION

Electrocatalytic CO_2 reduction (CO_2R) powered by renewable energy provides a sustainable, low-carbon pathway for producing value-added chemicals.[1,2] While progress has been made on C_{1-2} and C_{3+} oxygenate products,[3–5] the electrosynthesis of C_{3+} hydrocarbons remains challenging and mechanistically elusive.[6] To target these higher-value products, multi-element catalysts present an opportunity for novel catalytic properties through synergistic interactions among constituent elements.[7–9] Yet, traditional Edisonian trial-and-error approaches face challenges in efficiently exploring the enormous search space of the periodic table—not only in identifying effective compositions but also in elucidating the underlying design principles of multi-element systems.

Recent breakthroughs in robotics, automation, and high-throughput experimentation are accelerating the discovery of novel materials, enabling remarkable progress in molecular discovery.[3,10–13] However, adapting these advancements to heterogeneous electrocatalysts requires the production of extensive datasets. This task is challenging due to the complexity of preparing diverse catalysts and assessing their performance with sufficient throughput capacity, particularly under practical electrolyzer conditions.[2,14,15] While probabilistic artificial intelligence (AI) models offer advantages in addressing sparse-data challenges, traditional active-learning approaches that operate autonomously can converge prematurely to local optima, limiting their potential in identifying high-performance materials.

Integrating expert knowledge has demonstrated improved efficiency in search guidance,[16,17] providing an opportunity to overcome this limitation. Furthermore, AI models that are adaptive to domain expertise, combined with an accelerated experimentation platform that generates practically transferable datasets, offer additional potential for effective catalyst discovery[18]—especially within a high-dimensional material composition landscape typical of multi-electron catalytic processes.

In this work, we present an accelerated discovery workflow for multi-element CO_2 electrocatalyst for C_3 hydrocarbon electrosynthesis through an interactive human-in-the-loop approach. An editable glass-box machine learning (ML) model incorporates on-the-fly domain knowledge from human experts to refine anomalous predictions and guide an accelerated experimentation workflow that encompasses catalyst synthesis and CO_2R evaluation under practical membrane electrode assembly (MEA) configuration. This combined approach enables a ~165× acceleration compared with the conventional Bayesian-guided batched screening method, leading to the discovery of $Cu_{0.98}In_{0.02}$—the most effective composition to produce propylene, a critical chemical feedstock with a global annual capacity of 150.3 Mt. Furthermore, a data-driven analysis of the collected 300-composition dataset highlights two mechanistic branches that govern C_3 hydrocarbon production across multi-element compositions. An in-depth analysis of the $Cu_{0.98}In_{0.02}$ catalyst validated the effectiveness of this workflow at a device scale, achieving a propylene production rate of 6.0 mA cm^{-2} on a 25 cm^2 MEA (corresponding to 41.6 mmol g_{cat}^{-1} h^{-1}) under pH-neutral conditions. Comprehensive structural and *operando* spectroscopic analyses revealed that dilute In incorporation enhances both *CO dimerization and key intermediate stabilization toward propylene production, corroborating the data-driven mechanistic insights.

RESULTS

Search space definition

To define the multi-element catalyst design space for C_3 hydrocarbon production, we selected 15 elements to create unary, binary, and ternary compositions (Figure 1A). The selection was informed by previous CO_2R research and metallic phase stability under neutral CO_2R Pourbaix conditions, ensuring stable metallic states during CO_2R. This Pourbaix stability is crucial for intermediate adsorption energy-based feature engineering and subsequent ML modeling, as discussed later in the text (see Methods S1 for detailed rationale).

Accelerated experimental workflow for multi-element CO_2 electrocatalysts

The accelerated experimentation workflow for exploring multi-element CO_2 electrocatalysts is illustrated in Figure 1B. We conducted automated synthesis within a predefined chemical space using a Chemspeed SWING XL platform equipped with robotic tools (Figure S2A). We synthesized the powder catalysts by mixing metal precursors and then adding a reducing agent and purifying through repeated centrifugation and deionized (DI) water rinsing (Figure S2B). The fully automated workflow synthesized 60 catalysts in ~28 h (Video S1), which is accelerated by a factor of 34.1× compared with manual synthesis. This assessment was based on acc(X)eleration performance indicators (XPIs), a well-known set of metrics for gauging the effectiveness of an accelerated workflow.[19] For this purpose, we conducted a quantitative evaluation of the actual throughput achieved and the concurrent human costs (see detailed acceleration performance assessment in Methods S2). The automated workflow ensures high repeatability, as evidenced by consistent results obtained from repeated syntheses (Figure S3), mitigating the variability associated with conventional manual laboratory synthesis. We then prepared catalyst inks on the Chemspeed platform again and drop-cast onto 1 cm^2 gas-diffusion layers (GDLs) in an automated platform.[20,21] The drop-casted electrodes showed uniform catalyst layers. The electrodes also achieved CO_2R performance comparable to literature benchmarks obtained using commercial Cu nanoparticles across three independently prepared electrodes showing reliable reproducibility (Figure S4).[22]

To accelerate CO_2R performance evaluation and generate datasets transferable to industrially relevant conditions, we re-engineered conventional electrolyzer and measurement protocols with a parallelized 10× MEA platform (Figure S5) that features a custom-designed MEA with simple hold-down clamps (Figure S6A). This design enables rapid and simplified assembly while ensuring consistent electrode compression, supporting uniform performance across all parallel MEAs (Figure S7), and achieves CO_2R performance comparable to conventional MEA cells (Figures S6B and S6C).[23] To streamline gas product analysis from the parallel MEA operation, which is the major throughput-determining step of the end-to-end CO_2 electrocatalyst evaluation workflow, the 10× MEA platform integrates a gas

Please cite this article in press as: Kim et al., Accelerated discovery of CO_2-to-C_3-hydrocarbon electrocatalysts with human-in-the-loop, Joule (2025), https://doi.org/10.1016/j.joule.2025.102213

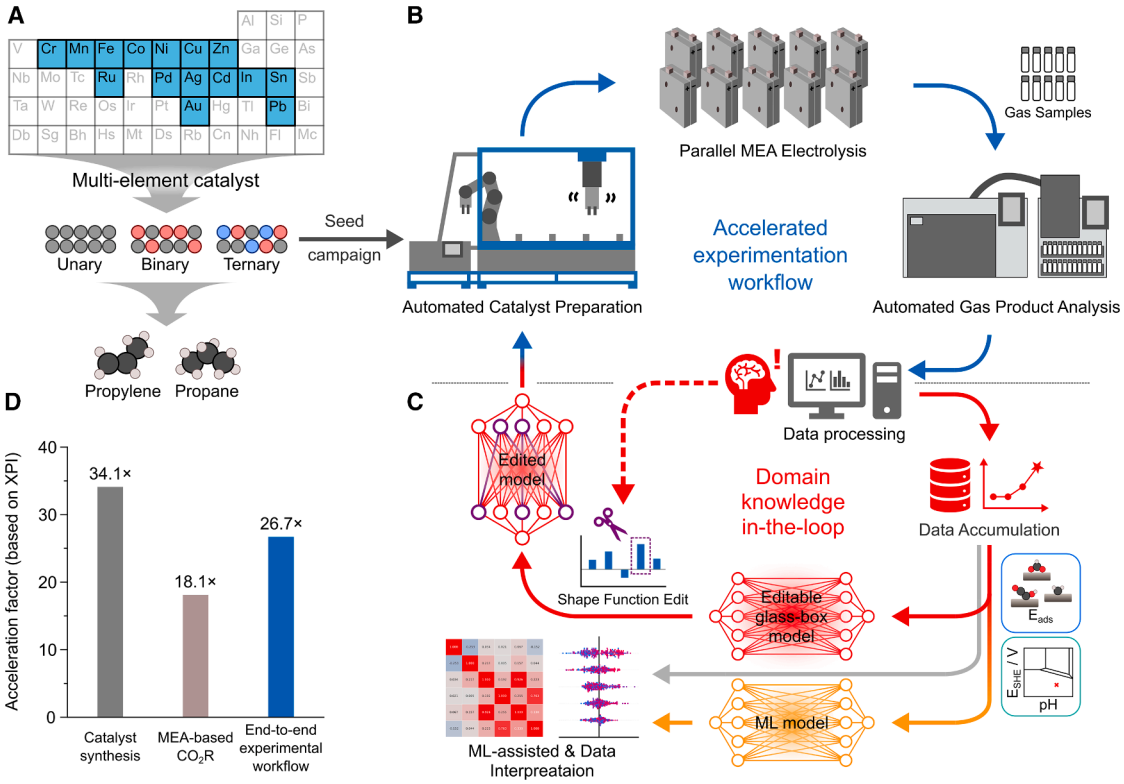

Figure 1. Overview of the study and accelerated workflow for multi-element CO_2 electrocatalyst exploration

(A) Compositional search space comprising 15 elements, investigating unary, binary, and ternary combinations to optimize CO_2 to C_3 hydrocarbons (propylene and propane).

(B and C) Schematic representation of the accelerated exploration workflow. (B) Beginning with the seed campaign compositions, the workflow integrates automated catalyst preparation (detailed robotic configuration in Figure S2A), a parallelized MEA-based CO_2 electrolyzer system (detailed description in Figure S5), and gaseous product analysis via automated GC. (C) Following each accelerated experimental round, an editable glass-box ML model was employed to train on accumulated experimental data, with target shape functions interactively refined through human domain expertise.

(D) Acceleration factors comparing the accelerated experimental workflow to conventional laboratory-based approaches for catalyst preparation, MEA-based CO_2R evaluation, and overall end-to-end experimental workflow. Acceleration factors were calculated using XPIs (see Methods S2 for detailed calculation) from the previous report.[18]

sampling station connected to each cathode outlet where gas products were collected using capped vials (Figure S5B). This allows decoupling of product sampling during MEA operation and subsequent gas chromatography (GC) analysis in full automation, making the workflow more labor-efficient while achieving actual high-data throughput. In three rounds of parallel operation under pH-neutral conditions (0.1 M $KHCO_3$), we evaluated 30 catalysts, yielding 90 gas sample vials (30 catalysts × 3 current densities) in 2.1 h (Figure S8). We then undertook automated GC analysis (see methods and Methods S3 for a detailed description of the accelerated CO_2R platform), resulting in an acceleration by a factor of 18.1× (Methods S2).

We determined the overall acceleration in experimentation by the end-to-end workflow, encompassing synthesis, electrode preparation, CO_2R testing, and idle time. Accounting for real-world experiment conditions in weekly data throughput and human cost (Figure S11), we assessed the acceleration in end-to-end experimental workflow as 26.7× (Figure 1D; Methods S2), facilitating rapid exploration of the vast multi-element compositional space.

Seed data campaign and chemical insights

We first initiated an exploratory seed campaign within the 15-element compositional search space, focused on C_3 hydrocarbon production, and generated a dataset of 15 unary catalysts and 105 equiatomic binary catalysts (e.g., $Cr_{0.50}Mn_{0.50}$). This minimal 120-sample design observes each element both alone and uniquely paired with every other element, enabling the ML model to identify first-order and pairwise effects from the outset. The heatmaps in Figure 2 illustrate the Faradaic efficiency (FE) for propylene (Figure 2A) and propane (Figure 2B) across the seed dataset. Catalysts showing high propylene production (magenta dashed box) were predominantly Cu-containing compositions—unary Cu and binary compositions containing Pd, Ag, and Sn—with negligible activity toward propane ($FE_{propane} < 0.01\%$). By contrast, catalysts with notable propane activity also produced propylene (purple dashed box) and were predominantly non-Cu-based compositions—unary Co and binary compositions of Mn or Fe combined with Ag, Cd, In, or Sn.

The contrasting trends between Cu-based and non-Cu-based compositions are emphasized in Figure 2C. The two distinctive

Please cite this article in press as: Kim et al., Accelerated discovery of CO_2-to-C_3-hydrocarbon electrocatalysts with human-in-the-loop, Joule (2025), https://doi.org/10.1016/j.joule.2025.102213

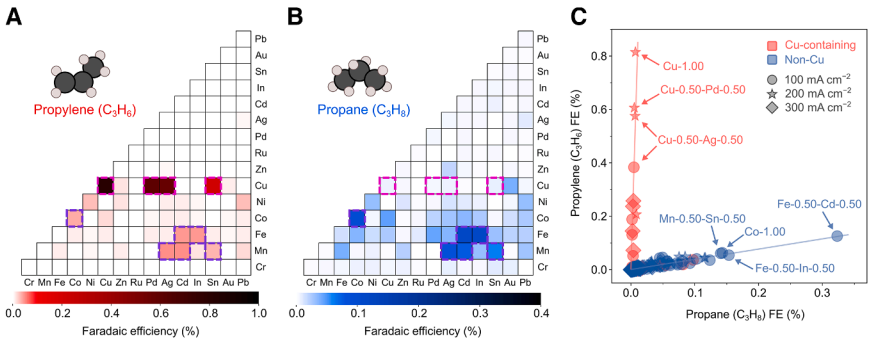

Figure 2. Seed dataset: FE for propylene and propane

(A and B) Heatmaps showing FE for propylene (A) and propane (B) at a current density of 200 mA cm^{-2}. Data obtained from the seed campaign. Highlighted regions indicate equiatomic compositions with notable activity toward propylene (magenta dashed box, $FE_{propylene} > 0.20\%$) and propane (purple dashed box, $FE_{propane} > 0.05\%$). (C) Scatterplot illustrating the relationship between propane and propylene FEs for Cu-containing and non-Cu catalysts at three different current densities.

trends in the FEs of propylene and propane, along with established CO_2R mechanistic pathways from prior studies (Figure S12),[24–26] suggest two pathways governing C_3 hydrocarbon production. For the Cu-containing catalysts, since C–C bond formation predominantly occurs through *CO dimerization step,[24,27] we hypothesized that this pathway is responsible for producing notable propylene with negligible propane (red line in Figure 2C). By contrast, for non-Cu catalysts, the linear correlation between propylene and propane production suggests C_3 hydrocarbon forms through *CH_x intermediates (following *CO to *CHO conversion[28]) and their subsequent coupling to produce both C_3 hydrocarbons.

Iterative data acquisition guided by on-the-fly domain knowledge

Active learning often faces a cold-start problem where early ML predictions are unreliable due to insufficient and imbalanced training data.[18,29] To overcome these challenges in exploring the 15-element space, we acquired a seed dataset, which was then used to initiate a chemical space search campaign. This campaign was driven by an editable ML model whose weights can be modified in an interpretable fashion to inject domain expertise into the model, as illustrated in Figure 1C. This approach employs an editable glass-box ML algorithm based on generalized additive models (GAMs).[30,31] Given an input $x \in \mathbb{R}^M$ and a target $y \in \mathbb{R}$, a GAM takes the form[32]:

$$g(\mathrm{E}(y)) = \beta_0 + \sum f_i(x_i)$$

where g is a link function, $\mathrm{E}(y)$ represents the expected value of the target y, and β_0 is the intercept constant. Here, each $f_i(x_i)$ represents an editable shape function, which captures the individual contribution of feature x_i to the predicted outcome. This editable architecture enables domain experts to directly inspect, modify, and refine individual shape functions that encode domain knowledge, thereby facilitating transparent and knowledge-guided exploration across diverse application domains, including electrochemical systems.

Prediction error is known to increase with model complexity,[33,34] and this relationship is accentuated when data is limited due to the propensity to overfit. Classifiers only need to estimate decision boundaries compared with regression's need to model precise continuous relationships, making them more suitable in the limited data regime. Hence, we trained a GAM-based binary classifier after each experimental round with a defined propylene partial current density ($j_{propylene}$) threshold. We selected propylene as the metric because it is commonly produced by catalysts generating C_3 hydrocarbons in both Cu-containing and non-Cu compositions (Figure 2B). To be able to intuitively interpret the model and refine its shape functions based on on-the-fly domain knowledge gleaned from the dataset, we built two types of descriptors. The first consists of categorical features that capture compositional information, and the second consists of thermodynamic features derived from CO_2R intermediate adsorption energies (E_{ads}). E_{ads}-based descriptors are readily obtained via AdsorbML pipeline[35]—which employs ML potentials with single-point density functional theory (DFT) calculations to estimate stable adsorbate-surface configurations—bypassing traditional, expensive DFT and making large-scale featurization accessible[35,36] (see Methods S4 for detailed feature engineering).

We then refined the model through GAM Changer,[37] an interactive graphical user interface enabling visualization and direct adjustment of shape functions (purple dashed line in Figures 1C and S13). For example, in the first iteration after the seed campaign, the seed dataset observation and hypothesis guided us to assign higher shape-function values to categorical element features associated with notable C_3 activity (Figure S14A). For E_{ads}-based continuous descriptors, we modified shape functions of interest—specifically, decreasing stepwise with increasing $E_{CO^*COH} - 2E_{*CO}$ and $E_{*CHO} - E_{*CO}$ values (Figure S14B)—to reflect the hypothesis that both *CO dimerization and *CO to *CHO conversion pathways contribute to C_3 hydrocarbon formation. We selected compositions for subsequent experimental rounds based on predictions from the refined models. A detailed description of the domain knowledge-in-the-loop framework is provided in Methods S4 and S5.

We executed this data acquisition campaign over five main iterations, each testing 30 new compositions by gradually increasing the classification threshold (Figure 3A, bottom graph) and progressively shifting from exploration to exploitation. Detailed records of shape-function modification, sampling policy, and the underlying on-the-fly domain knowledge are detailed in Methods S5 and Table S4. Models refined with domain knowledge showed better predictive capabilities with higher F_1 scores compared with the initial models (bottom graph of Figure 3A and confusion matrices in Figure S15), which supports the effectiveness of human-in-the-loop knowledge integration. This

Please cite this article in press as: Kim et al., Accelerated discovery of CO_2-to-C_3-hydrocarbon electrocatalysts with human-in-the-loop, Joule (2025), https://doi.org/10.1016/j.joule.2025.102213

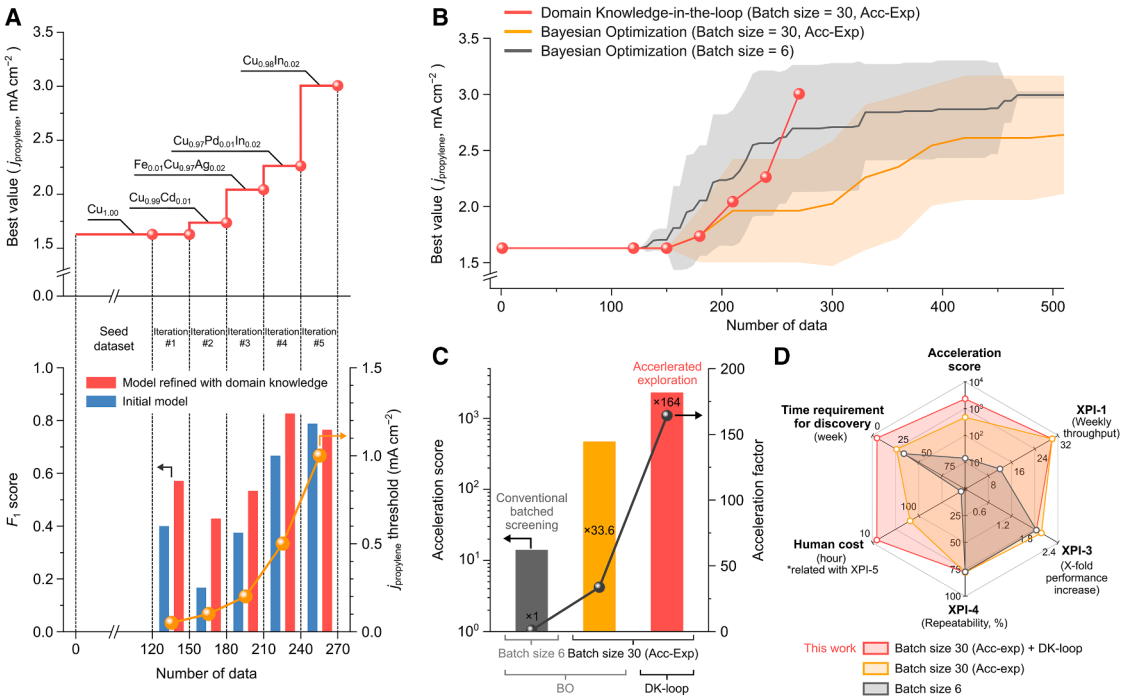

Figure 3. Human domain knowledge-in-the-loop data acquisition using an editable glass-box ML model

(A) Top: performance evolution through the domain-knowledge-guided iterations, highlighting the maximum propylene partial current density achieved after each sequential batch. Bottom: comparative analysis of F_1 scores between classification models with and without domain knowledge-guided edits across successive data acquisition batches, with progressively increasing $j_{propylene}$ thresholds (yellow line).

(B) Comparison of three exploration strategies on the virtual composition-$j_{propylene}$ space derived from a surrogate model trained on the complete experimental dataset. Shaded regions represent standard deviations from ten independent emulated experiments.

(C) Acceleration score comparison calculated using XPIs across different exploration strategies with acceleration factors normalized to conventional batched screening (BO with batch size = 6), demonstrating relative efficiency gains between conventional batched experiments and the accelerated exploration approach.

(D) Radar chart visualization of individual XPI contributions to the overall acceleration score, comparing four different exploration strategies (see Methods S6 for detailed description and calculation). DK-loop denotes domain knowledge-in-the-loop.

advantage enabled rapid identification of a catalyst with high CO_2-to-propylene activity—$Cu_{0.98}In_{0.02}$—in merely five iterations (Figure 3A, top graph). Specifically, through iterations 1–3, domain knowledge refinement consistently improved both precision and recall (Figure S16), while exploration identified Ag, Fe, Pd, Cd, and In as promising dopants for Cu (iteration 3; Methods S5). In iteration 4, the refined model correctly identified all 10 high-performing compositions with only 2 false positives, providing confidence for targeted exploitation. The subsequent discovery of $Cu_{0.97}Pd_{0.01}In_{0.02}$ (2.262 mA cm^{-2} in iteration 4) along with $Cu_{0.95}In_{0.05}$ (1.285 mA cm^{-2} in iteration 3) further validated the potential of trace In doping, ultimately leading to the $Cu_{0.98}In_{0.02}$ discovery in iteration 5. The effectiveness of this approach was further confirmed when F_1 scores converged between pre- and post-refinement models in iteration 5, indicating that the expanded dataset had effectively internalized the domain knowledge patterns.

Performance benchmarking of accelerated exploration

To assess the effectiveness of integrating accelerated experimentation with domain knowledge-guided ML, we simulated experiments on a virtual composition-$j_{propylene}$ space derived from a surrogate model trained on the experimental dataset (Figure 3B). We specifically focused the benchmarking on composition-exploration, which is particularly time-intensive in catalyst development. Under realistic laboratory conditions, a conventional batched screening approach (batch size = 6, a conservative estimate of 12 catalysts per week—a challenging but generous baseline for conventional campaigns) guided by Bayesian optimization (BO) would require ~34 weeks to discover a catalyst with $j_{propylene}$ > 3.0 mA cm^{-2}, assuming achievable weekly data throughput (Figures S11 and S18) with an XPI-based overall acceleration score[17] of 14.1 (relative to BO with batch size = 1; see detailed acceleration score calculation in Methods S6). By contrast, applying BO with accelerated experimentation (batch size = 30) increases the acceleration score to 474.0, a 33.6× acceleration over conventional batched screening—largely due to enhanced data throughput and reduced human cost (Figure 3D). Notably, this accelerated exploration strategy achieves an acceleration score of 2,314.0, representing an additional 4.9× acceleration over the batch size of 30 with the BO approach. We attribute this further enhancement to more efficient data acquisition through incorporation of domain knowledge into the iterative loop. In summary,

Please cite this article in press as: Kim et al., Accelerated discovery of CO_2-to-C_3-hydrocarbon electrocatalysts with human-in-the-loop, Joule (2025), https://doi.org/10.1016/j.joule.2025.102213

both the novel experimentation platform and human domain knowledge-guided machine intelligence contributed to rapid catalyst discovery, resulting in a ~165× acceleration relative to conventional Edisonian-like batched screening.

Data-driven mechanistic inference across multi-element compositions

Using the compiled dataset, we also sought to elucidate compositional design principles governing C_3 hydrocarbon production. The final dataset of 300 data points confirms the trends observed in the seed dataset: catalysts with high propylene activity are Cu-containing, whereas those with notable propane activity are mainly non-Cu-based (Figure S19A).

To understand this behavior, we performed Pearson correlation analyses to quantify the relationships among CO_2R products. Figure 4A shows that in Cu-containing catalysts—mainly active toward propylene—$FE_{propylene}$ strongly correlates with $FE_{ethylene}$. By contrast, broad intercorrelations among all C_{1-3} hydrocarbons are observed in non-Cu catalysts (Figure 4B). Since strong correlation indicates shared reaction intermediates and mechanistic pathways,[38] these findings corroborate the hypothesis from observing the seed dataset: propylene production in Cu-containing catalysts shares a mechanistic pathway with ethylene formation, while C_{1-3} hydrocarbon production in non-Cu systems is intercorrelated, strongly suggesting shared $*CH_x$ intermediates.

To further investigate these correlation-based mechanistic insights for C_3 hydrocarbon production, we conducted ML-assisted analysis with E_{ads}-based descriptors. We first evaluated possible stable phases under neutral CO_2R conditions via Pourbaix analysis[39] and incorporated E_{ads} of key intermediates on these phases[35] to build CO_2R pathway-related descriptors (see Methods S7 for detailed description). With these descriptors, we implemented gradient boosting models in XGBoost to predict C_3 hydrocarbon production (Figure 4C for propylene and Figure S21 for propane). We then performed Shapley additive explanations (SHAP) analysis, using leave-one-out cross-validation (LOOCV) to quantify how specific CO_2R pathway-related features influence product formation.

For both propylene and propane production, $E_{*CHO} - E_{*CO}$ emerged as the most critical descriptor but with inverse contributions (Figures 4D and 4E), representing a robust pattern of feature importance and directional trends across independent training runs (Figure S22). For propane-active catalysts, lower $E_{*CHO} - E_{*CO}$ values—indicating thermodynamically favorable *CO to *CHO conversion—correlate with enhanced activity (Figure 4E). This correlation supports interrelated C_{1-3} hydrocarbon formation via $*CH_x$, which is consistent with previous reports identifying *CO to *CHO conversion as the rate-determining step, followed by proton-electron transfers to form *CH, $*CH_2$, and $*CH_3$.[27,28] Non-Cu compositions that show notable propane activity include Co, Mn, and Fe (Figure S19B), which are renowned catalysts (Fe[40,41] and Co[41,42]) or promoters (Mn[43]) for Fischer-Tropsch synthesis (FTS), excelling at stabilizing $*CH_x$ during hydrocarbon chain growth. Although CO_2R is an electrochemical process, this parallel between propane-active non-Cu system and FTS catalysts suggests a similar $*CH_x$-mediated pathway with $*CH_x$ coupling, producing propane and intercorrelated C_{1-3} hydrocarbons from CO_2R. Examining the top-performing compositions for propane in the dataset, we found that combining Fe, Co, and Mn with elements that drive CO_2 to formate conversion (Sn, Cd, In, and Pb) improved propane production. Additionally, low E_{*COOH} emerged as the second most important feature for propane production, indicating that stable *COOH binding (low E_{*COOH}) improves propane formation. This trend was particularly pronounced when the training dataset was restricted to non-Cu catalysts (Figure S23), underscoring its significance in non-Cu systems and suggesting that *COOH may be involved in hydrocarbon production pathways alongside $*CH_x$.

By contrast, for propylene activity, higher $E_{*CHO} - E_{*CO}$ values achieve high propylene production (Figure 4D). This observation aligns with previous reports that unfavorable *CHO formation from *CO is one factor that facilitates C–C coupling via *CO dimerization,[44] supporting the hypothesis that high propylene production originates from the *CO dimerization pathway. SHAP analysis further identified unfavorable *OCHO formation (high E_{*OCHO}) as the second most important feature for propylene production. Given the three major pathways for CO_2 at the catalyst surface (direct adsorption as $*CO_2$, conversion to either *COOH or *OCHO through concerted proton-electron transfer) and that the third important feature (lower E_{*COOH}) positively influences propylene production, we deduce that *COOH could also be relevant to propylene production. Other individual E_{ads} (E_{*CO}, E_{CO*COH}, E_{*CHO}, and E_{*C}) did not show significant SHAP importance for either propylene or propane production when included in the model (Figure S24).

To sum up, we highlight potential mechanistic pathways toward C_3 hydrocarbon formation across multi-element compositions in Figure 4F. The data-driven interpretation also encompasses findings from previous reports, based on systematic in-depth studies of individual catalysts.[38,45] This approach combines accelerated experimentation and ML to extract generalized mechanistic insights from a wide range of multi-element compositions targeting C_3 hydrocarbons.

Scalability and mechanistic validation of the champion catalyst

We applied conventional methods to validate the scalability and practical applicability of the champion composition ($Cu_{0.98}In_{0.02}$) identified through the accelerated workflow. Leveraging the facile synthesis protocol employed on the automated platform, we manually synthesized $Cu_{0.98}In_{0.02}$ at 1,500 times the original scale (Figure S25). This approach yielded 20.2 g of the catalyst, demonstrating feasibility for larger-scale applications (Figure 5A inset). Transmission electron microscopy (TEM), energy-dispersive X-ray (EDX) spectroscopy (Figure 5A), and X-ray photoelectron spectroscopy (XPS) revealed the presence of both Cu and In peaks in $Cu_{0.98}In_{0.02}$, while only Cu signals were observed in $Cu_{1.00}$ (Figures 5B and 5C). We further quantified the atomic composition of $Cu_{0.98}In_{0.02}$ with X-ray fluorescence (XRF) analysis, which showed Cu and In content of 98.5 atom % and 1.5 atom %, respectively. High-resolution X-ray diffraction (XRD) coupled with Rietveld refinement revealed that the catalyst consists of a heterostructure of metallic Cu (98.4 wt %), Cu_2O (1.3 wt %), and $In(OH)_3$ (0.3 wt %) (Figures 5D and S26A). With bulk compositional analysis (XRF) and surface-sensitive analysis

Please cite this article in press as: Kim et al., Accelerated discovery of CO_2-to-C_3-hydrocarbon electrocatalysts with human-in-the-loop, Joule (2025), https://doi.org/10.1016/j.joule.2025.102213

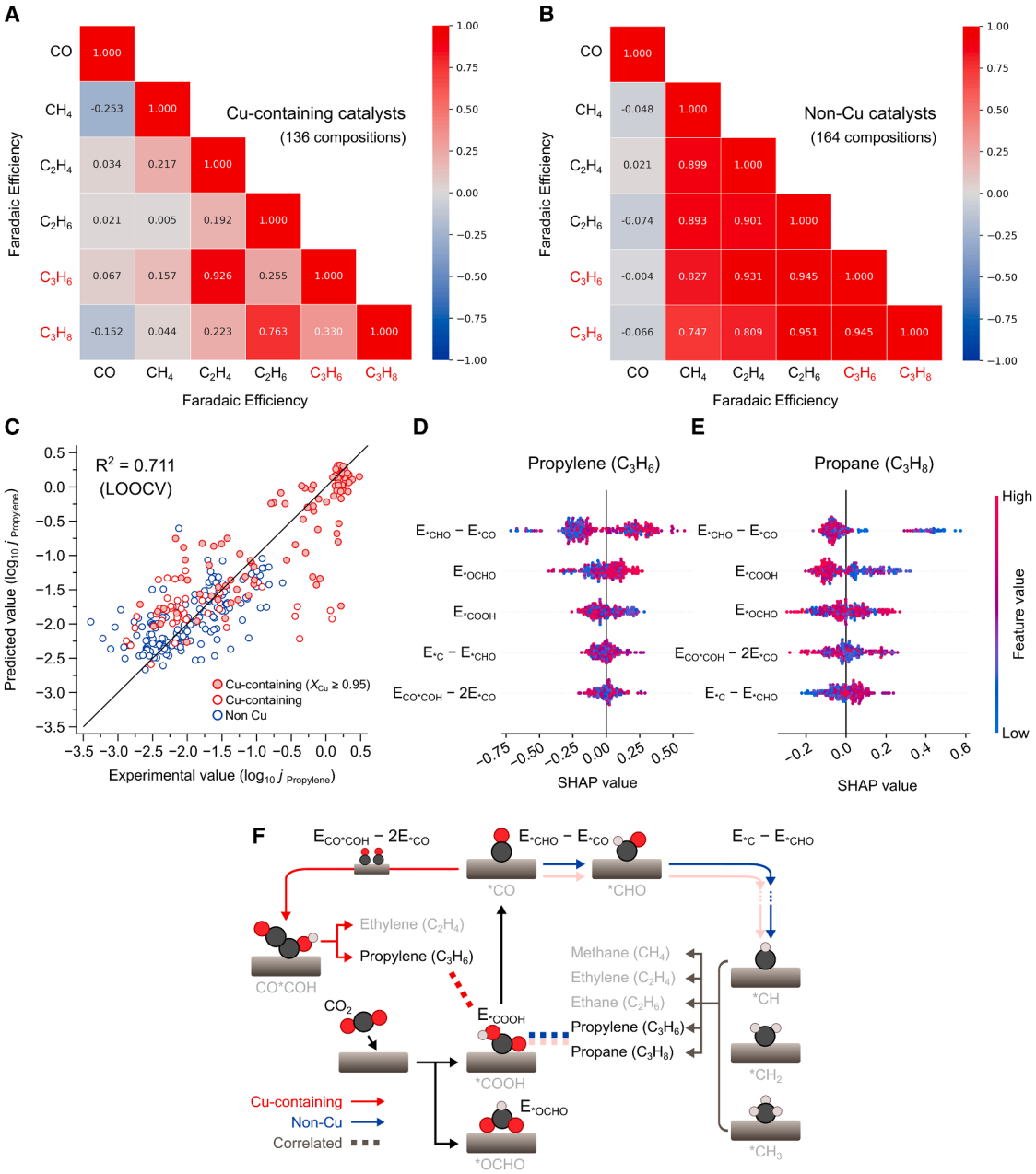

Figure 4. Analysis of catalyst performance for propylene and propane production through experimental data interpretation and ML-assisted approaches

(A and B) Pearson correlation matrix between FEs of gaseous products during CO_2R for Cu-containing catalysts (A) and non-Cu catalysts (B). Red indicates positive correlation and blue indicates negative correlation, with color intensity reflecting correlation strength.

(C) Correlation between experimentally observed and predicted $\log_{10} j_{propylene}$ values for the entire dataset, showing $R^2 = 0.711$ and $r_{Pearson} = 0.843$, evaluated using LOOCV.

(D and E) SHAP analysis of E_{ads}-based descriptors for predicting propylene (D) and propane (E) production rates across the complete dataset. Color gradients indicate descriptor values, while SHAP values quantify each descriptor's contribution magnitude and direction.

(F) Proposed CO_2R pathways toward C_3 hydrocarbon production, illustrating mechanistically distinct routes toward propylene and propane formation in Cu-containing and non-Cu catalysts.

(XPS), the results indicate that In is incorporated predominantly as a dilute solid solution within the Cu matrix—as indicated by the color contrast of the catalyst powder compared with $Cu_{1.00}$ (Figure S26B)—while a minor $In(OH)_3$ phase (<7.9% of total In content) is localized at the catalyst surface (see detailed analysis in Methods S8).

Please cite this article in press as: Kim et al., Accelerated discovery of CO_2-to-C_3-hydrocarbon electrocatalysts with human-in-the-loop, Joule (2025), https://doi.org/10.1016/j.joule.2025.102213

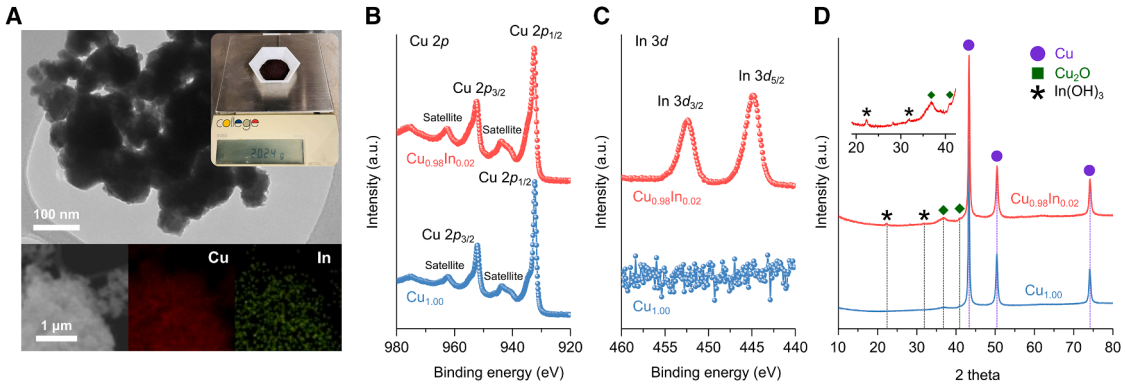

Figure 5. Physicochemical characterization of the discovered $Cu_{0.98}In_{0.02}$ catalyst

(A) TEM image and EDX spectroscopy elemental mapping of Cu and In distribution. The inset shows a photograph of the catalyst obtained via 1,500× scaled-up synthesis.

(B and C) XPS spectra showing Cu 2*p* (B) and In 3*d* (C) signals for $Cu_{0.98}In_{0.02}$ and $Cu_{1.00}$ catalysts.

(D) XRD patterns of $Cu_{0.98}In_{0.02}$ and $Cu_{1.00}$ catalysts.

We then evaluated the CO_2R performance in a commercial MEA electrolyzer with an active area of 25 cm^2, using 0.1 M $KHCO_3$ as the anolyte. Figure 6A shows the $Cu_{0.98}In_{0.02}$ catalyst achieved an $FE_{propylene}$ of 2.0% at 300 mA cm^{-2} (geometric current density of 6.0 mA cm^{-2}), corresponding to a propylene production rate of 41.6 mmol g_{cat}^{-1} h^{-1} at a full-cell voltage of −3.47 V (without compensating for ohmic losses; Figure 6B). Considering that propylene production in Cu-containing catalysts shares a pathway with ethylene via *CO dimerization, a comparison of the $FE_{propylene}$:$FE_{ethylene}$ ratio between $Cu_{0.98}In_{0.02}$ and $Cu_{1.00}$ suggests that In doping enhances selectivity toward propylene over ethylene, especially at higher current densities (Figure 6C). The identified $Cu_{0.98}In_{0.02}$ catalyst outperforms previous reports in propylene electrosynthesis (Table S6) under industrially relevant conditions, operating a scaled-up MEA at practical current density.[2] The catalyst exhibited sustained performance in the 25 cm^2 MEA over 30 h (Figure S27A). Post-mortem TEM and EDX analyses reveal particle aggregation relative to the initial state; however, the dilute incorporation of In within the Cu matrix remains largely preserved (Figure S27C). These results highlight the promise of the catalyst discovery workflow in rapidly delivering candidates for scaled synthesis and device-level performance validation. However, further improvements in long-term durability—extending to >500 h of continuous operation[2]—remain an important target for practical implementation. Such efforts should be pursued through device-level optimization (Figure S27B), building on the rapid compositional screening framework demonstrated in this work.

To elucidate the origin of the enhanced propylene production in $Cu_{0.98}In_{0.02}$, we performed *operando* Raman spectroscopy[46,47] (Figure 6D) and flow-cell electrocatalysis with varied feed conditions—CO_2, CO, and a CO+HCOOK co-feed[45] (Figure 6E). *Operando* Raman measurements revealed that $Cu_{0.98}In_{0.02}$ exhibited a higher proportion of high-frequency relative to low-frequency $CO_{ads\ (atop)}$ species in the 1,950–2,100 cm^{-1} range compared with $Cu_{1.00}$ (Figure 6D). This, along with the higher $CO_{ads\ (stretch)}$/$CO_{ads\ (rotation)}$ ratio in the ∼280–360 cm^{-1} region, indicates a higher coverage of CO* with favorable binding energies for C–C coupling,[5,48–50] which is consistent with its higher C_2H_4 production rate under CO reduction (COR) (Figure 6E).

At identical potentials, the propylene production rate under CO_2R exceeded that under COR for both catalysts (Figure 6E). Considering the mechanistic linkage between the CO_2 and CO feeds (CO_2 → *COOH → *CO), this disparity implicates a pre-*CO intermediate—*COOH, *OCHO, or both—in the propylene formation pathway. To probe the intermediate identity, we co-fed formate (HCOOK) with CO.[45] The propylene production rate did not appreciably increase relative to CO alone for either catalyst, indicating a limited role for *OCHO and supporting *COOH as the more relevant precursor.[38] Additionally, *operando* Raman spectra of $Cu_{0.98}In_{0.02}$ show more pronounced peaks at ∼1,340 and ∼1,540 cm^{-1} than those of $Cu_{1.00}$. These features are characteristic of the symmetric and asymmetric carboxylate stretching modes, attributed to activated CO_2-derived species rather than spectator (bi)carbonate.[51] The intensity of these peaks decreased at more negative current density (−30 mA cm^{-2}), while a new peak emerged at ∼1,450 cm^{-1}—previously attributed to the *OCCO intermediate together with the 1,550 cm^{-1} band[5,52]—indicating formation of C–C coupled intermediates. These observations suggest that the ∼1,340/1,540 cm^{-1} pair is associated with carboxylate intermediates potentially derived from *COOH formed under locally alkaline conditions. These features are pronounced at lower current densities but attenuate at higher current densities as they are progressively consumed, evolving into C–C coupled intermediates.

Combined with structural characterization, these observations suggest that dilute incorporation of In into the Cu matrix ($Cu_{0.98}In_{0.02}$) strengthens two critical steps in the propylene formation pathway: *CO dimerization and *COOH stabilization. These enhancements are inferred to originate from the intrinsic properties of In—its larger atomic radius and lower electronegativity compared with Cu: (1) Cu *d*-band modulation weakens *CO binding, promoting $CO_{ads\ (atop)}$ (as evidenced by the emergence of high-frequency $CO_{ads\ (atop)}$ at ∼2,090 cm^{-1} for $Cu_{0.98}In_{0.02}$;

Please cite this article in press as: Kim et al., Accelerated discovery of CO_2-to-C_3-hydrocarbon electrocatalysts with human-in-the-loop, Joule (2025), https://doi.org/10.1016/j.joule.2025.102213

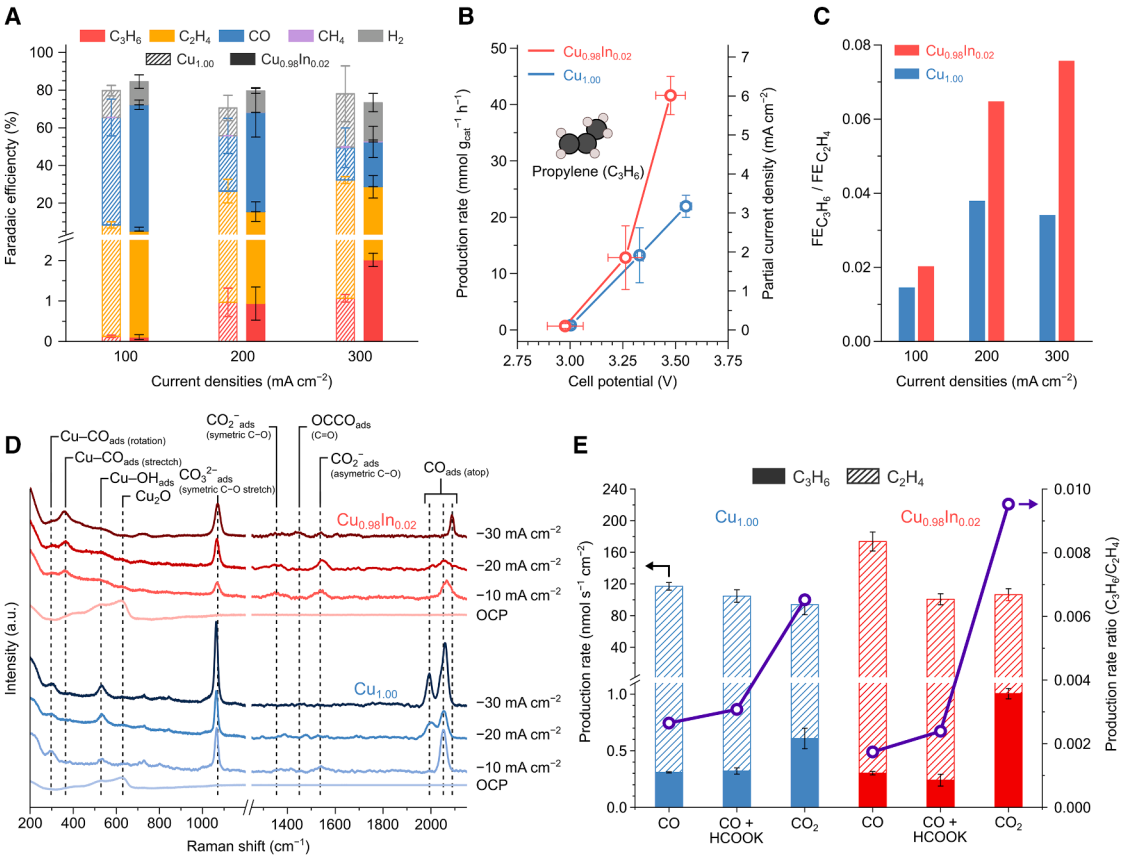

Figure 6. Electrochemical evaluation of the discovered $Cu_{0.98}In_{0.02}$ catalyst

(A) FE of gas products at three different current densities for both catalysts in a 25 cm^2 MEA electrolyzer under 0.1 M $KHCO_3$. Error bars represent the standard deviation from three independent measurements.

(B) Full-cell potential with corresponding propylene production rates (mmol g_{cat}^{-1} h^{-1}) and propylene partial current densities (mA cm^{-2}) Error bars represent the standard deviation from three independent measurements.

(C) Comparison of $FE_{propylene}/FE_{ethylene}$ ratio at different current densities. Error bars represent the standard deviation from three independent measurements.

(D) *Operando* Raman spectra of $Cu_{0.98}In_{0.02}$ and $Cu_{1.00}$ catalysts in contact with 0.1 M $KHCO_3$ electrolyte, collected under chronopotentiometric conditions at different applied current densities.

(E) Propylene and ethylene production rates and their ratio for $Cu_{0.98}In_{0.02}$ and $Cu_{1.00}$ catalysts, measured in a flow cell with 0.1 M KH_2PO_4 electrolyte at −1.5 V_{RHE}. Error bars represent the standard deviation from three independent measurements (RHE: reversible hydrogen electrode).

Figure 6D) that is more favorable for *CO dimerization,[48,53,54] and (2) the more electropositive and harder Lewis-acidic character of In provides enhanced stabilization of *COOH. The in-depth investigation of the champion catalyst is consistent with the ML-assisted mechanistic insights toward propylene production obtained from 300 compositions (Figure 4F). This convergence demonstrates the capability of the workflow to both extract transferable understanding across a large compositional space and accelerate the discovery of high-performance catalysts.

DISCUSSION

In this work, we demonstrated a method of accelerating the exploration of multi-element CO_2 electrocatalysts. We established an experimentation platform capable of generating quality datasets with high-data throughput capacity and integrated it with on-the-fly domain knowledge-guided machine intelligence. This approach enabled rapid navigation of a vast 15-element compositional space, achieving a ~165× acceleration compared with the conventional batched BO approach. Through comprehensive analysis, we inferred mechanistic insights across multi-element compositions: Cu-containing catalysts predominantly generate propylene via *CO dimerization, while non-Cu compositions produce C_{1-3} hydrocarbons through $*CH_x$-mediated pathways, with *COOH potentially relevant for both pathways. We validated the robustness of this approach through identifying practically viable catalysts by discovering a high-performance catalyst, $Cu_{0.98}In_{0.02}$, and demonstrating scalable performance. We further demonstrated successful scaled synthesis and performance of this catalyst in a 25 cm^2 MEA operation, achieving a propylene production rate of 6.0 mA cm^{-2} (41.6 mmol g_{cat}^{-1} h^{-1}) under pH-neutral conditions and exceeding previous performances in propylene electrosynthesis (Table S6). Combined physicochemical characterization

Please cite this article in press as: Kim et al., Accelerated discovery of CO_2-to-C_3-hydrocarbon electrocatalysts with human-in-the-loop, Joule (2025), https://doi.org/10.1016/j.joule.2025.102213

of $Cu_{0.98}In_{0.02}$, *operando* Raman spectroscopy, and electrochemical analysis suggest that dilute In incorporation into Cu promotes *CO dimerization and stabilizes *COOH—key precursors to propylene formation—thereby validating the data-driven mechanistic insights.

These findings suggest that future studies incorporating additional data on catalyst properties, their local microenvironment, and electrochemical behavior will enable more sophisticated feature engineering, as well as structural/morphology descriptors to decouple composition-correlated effects, further enhancing ML model predictability and interpretability. Maintaining notable data throughput under practical electrolyzer conditions while achieving full automation and integrating adaptive active-learning approaches that are responsive to knowledge gleaned from the data may help enable effective self-driving laboratories for heterogeneous catalysis systems. We also anticipate that this openly accessible dataset will facilitate novel discoveries in CO_2 electrocatalyst design by the broader scientific community, accelerating progress toward practical implementation of renewable carbon utilization technologies.

METHODS

Automated multi-element electrocatalyst synthesis

Automated high-throughput electrocatalyst synthesis was carried out using the Chemspeed SWING XL platform (Figure S2). Multi-element catalysts were synthesized via co-reduction of mixed metal precursor solutions, with a hydrazine/NaOH solution (hydrazine hydrate [Sigma Aldrich, 50%–60%]: NaOH [6 M]: DI water = 25:12:15, v/v) serving as the reducing agent. Initially, 0.15 M metal precursor stock solutions and the hydrazine/NaOH solution were manually prepared and positioned in the stock solution zone (see Table S7 for details of chemicals). The stock solutions were then combined in precise ratios to achieve the desired multi-element composition, maintaining a final volume of 1.5 mL per tube. For Cu-rich compositions ($x_{Cu} \geq 0.95$), stock solutions of secondary elements were prepared at 0.03 M (1/5 dilution of the standard 0.15 M) to minimize dispensing errors associated with small volume additions, and appropriate volumes were dispensed according to the target atomic ratios (i.e., in this case, the final volume deviates from 1.5 mL). For Ag-containing compositions, a powdered $AgNO_3$ precursor was used and dispensed directly into the tubes in precise amounts, with DI water added separately to address the instability issue of $AgNO_3$ stock solutions. After mixing thoroughly, the tubes were transferred to the shaker zone for 5 min to ensure homogeneity. Subsequently, the tubes were placed in a 50°C ultrasonic water bath, where 0.65 mL of hydrazine/NaOH solution was added dropwise during ultrasonication. The reaction proceeded under ultrasonication for 30 min, followed by an additional 30 min in the 50°C water bath. Upon completion, the tubes were capped and transferred to the centrifuge rack for centrifugation. The synthesized particles underwent three purification cycles, where the supernatant was removed, fresh DI water was added, and the tubes were ultrasonicated for 10 min per cycle. Each synthesis batch consisted of 15 tubes, allowing for the preparation of 15 distinct compositions per run, which required approximately 7 h. For the seed dataset containing 120 catalysts, the automated synthesis was performed in two rounds of 60 catalysts each, with each round taking approximately 28 h. Batch expansions (batches 1–6) involving 30 catalysts each required approximately 15 h per batch. Finally, the tubes were transferred to a vacuum oven and dried at 40°C for 12 h.

Automated catalyst ink and electrode preparation

Following vacuum drying, zirconia balls were added to each tube, and the samples were ball-milled for 10 min using a high-throughput vortex-vibration ball mill (MSK-SFM-50, MTI Corporation). After milling, the tubes were returned to the Chemspeed platform for automated catalyst ink preparation. Vulcan carbon XC-72R (Fuel Cell Store) and a Nafion/propanol solution (Nafion perfluorinated resin solution [Sigma Aldrich, 20 wt %]: 2-propanol [Sigma Aldrich, ≥99.5%] = 2.5:50, v/v) were added to each tube in a ratio of catalyst:carbon:propanol = 6 mg:4 mg:0.5 mL. The tubes were then capped and placed in an ultrasonic bath, where they were sonicated for 1 h to ensure uniform ink dispersion. To mitigate potential catalyst oxidation during this process, the water in the ultrasonic bath was drained and refilled with room-temperature water between the sonication of each batch. Each batch contained 15 tubes, and the entire preparation of 30 catalyst inks took approximately 2 h. The prepared catalyst inks were then drop-cast (50 μL) onto a 1 cm^2 GDL (Freudenberg H23C3, Fuel Cell Store) using an automated platform comprising an Opentrons liquid handler, ultrasonic bath with infrared interface (Bandelin, DT102 H-RC), and robotic arm.

Accelerated CO_2R performance evaluation

The parallel screening utilized a modified setup from the previous work for CO_2R evaluation (Figure S5). CO_2 gas (Linde, 99.99%) was supplied through individual DI water humidifiers to each cell at 30 sccm using 10× mass-flow controllers (Sensirion, SFC5500-0.5slm) via Python control. Each MEA cell (1.0 cm^2 active area) was assembled in layers: a 1 cm^2 cathode placed onto the cathode plate, followed by an activated anion-exchange membrane (Sustainion X37-50 Grade RT), an IrO_x/Ti mesh electrode (Magneto special anode), and the anode plate. The assembly was secured using a quick-lock hold-down clamp calibrated for consistent pressure through sputtered Cu (~750 nm thickness) sample CO_2R tests (Figure S7). Separate anolyte chambers supplied 0.1 M $KHCO_3$ to each anode. CO_2R performance of 10× MEAs was evaluated using a multichannel battery test system (Landt Instruments, CT3002A-9V1A) at current densities of 100, 200, and 300 mA cm^{-2}, with each 9-min cycle comprising 3 min for catalyst activation, 5 min for gas sampling, and a 1-min buffer. A dual-needle gas sampler stand enabled gas input and air purging (Figure 5B). The 5-min gas sampling period ensured sufficient air purging from the vials (Figure S8), with samples in PTFE (polytetrafluoroethylene)/silicone-capped vials maintaining stability for over 2 days with minimal leakage. Collected gas samples were then analyzed in an automated fashion using GC (PerkinElmer Clarus 590, equipped with thermal conductivity and flame ionization detectors) with a headspace autosampler (TurboMatrix HS110). The automated analysis system processed approximately 90

samples per day, with each chromatogram acquisition requiring 14 min. The resulting chromatograms were batch-processed to FEs using custom software and Python scripts. The code is available in the GitHub repository.

Adsorption energy data mining

Adsorption energies were mined from the Open Catalyst Project API using the ocpapi Python library.[34] We mined data for the intermediates *OCHO, *COOH, *CO, CO*COH, *CHO, and *C on specific material structures with Materials Project IDs, focusing on the Miller indices (100) and (211). For compositions that are not available in ocpapi, we directly employed the AdsorbML workflow, which begins by generating 100 initial adsorbate placements on a metal surface. These configurations are then relaxed using a pre-trained EquiformerV2 deep learning model, which rapidly optimizes the atomic positions to identify energetically favorable binding sites.[55] The workflow includes automated post-processing steps to identify and filter out anomalous configurations where the adsorbate has desorbed, dissociated, or significantly altered the surface structure. The maximum allowed force component (f_{max}) was set to 0.02, with optimization steps limited to 300. All code for adsorption energy mining is available in the GitHub repository.

Human-in-the-loop data acquisition

The engineered feature space comprised both compositional and adsorption energy-based descriptors, with detailed feature engineering explained in Methods S4. For each accelerated experimentation iteration, we established $j_{propylene}$ threshold values—which were progressively increased throughout successive iterations, as shown in Figure 3A. Based on these thresholds, we employed the explainable boosting machine (EBM) classifier, a modern implementation of the GAM framework.[29] The EBM model was optimized using grid search cross-validation with a hyperparameter space encompassing maximum leaves $\in$ [2, 3], smoothing rounds $\in$ [50, 75], learning rate $\in$ [0.005, 0.015], and interaction strength $\in$ [0, 0.9]. The optimization process utilized 5-fold cross-validation with the F_1 score as the performance metric. The trained EBM model's shape functions were subsequently edited through the GAMChanger interactive interface[36] to align with domain knowledge gleaned from the training data. Using this refined EBM model, we generated predictions across the search space and selected compositions for the subsequent experimental round (detailed procedures for refinement and sample selection are provided in Methods S5). Both pre-refinement and post-refinement EBM models were preserved and subsequently evaluated against experimental data in the following round, with comparative performance assessed using F_1 scores.

ML regression

The regression analysis was performed using the XGBoost library, an efficient implementation of gradient-boosted decision trees. The model was optimized through randomized hyperparameter search with 200 iterations using 5-fold cross-validation, evaluating root-mean-squared error (RMSE) as the performance metric. The hyperparameter space included the number of estimators (50, 500), maximum tree depth (2–10), learning rate (0.01–0.3), subsample ratio (0.6–1.0), column sampling ratio (0.6–1.0), minimum child weight (1–7), gamma (0–0.5), and L_1/L_2 regularization terms (0–1). Model performance was evaluated using LOOCV to maximize utilization of the available data while ensuring robust validation. In each LOOCV iteration, the model was trained on ($n - 1$) samples and tested on the held-out sample, where n represents the total number of samples. Final model performance was assessed using the coefficient of determination (R^2) and RMSE calculated across all LOOCV predictions. Additionally, SHAP analysis was performed on each test sample during the LOOCV process, with SHAP values aggregated across all n data points to quantify feature importance.

Scalable $Cu_{0.98}In_{0.02}$ synthesis and conventional CO_2R performance evaluation

For the scalable synthesis of $Cu_{0.98}In_{0.02}$ catalyst, the automated synthesis protocol was scaled up 1,500-fold, using 77.46 g of $Cu(NO_3)_2{\cdot}3H_2O$ and 2.03 g of $In(NO_3)_3{\cdot}xH_2O$ in 2.25 L of DI water. After heating the solution to 50°C through a water bath, 975 mL of hydrazine/NaOH solution (prepared following the aforementioned recipe) was slowly added. The reaction was conducted with stirring (900 rpm) for 30 min, followed by 30 min of static conditions to complete the reaction. The catalyst was then collected via filtration, repeatedly washed with DI water, and dried in a vacuum oven at 40°C for 12 h. Following the automated ink preparation protocol as described above, the catalyst ink was prepared and spray-coated onto a 5 × 5 cm GDL (Freudenberg H23C3, Fuel Cell Store) with a loading of 0.3 mg cm^{-2} catalyst and 0.2 mg cm^{-2} Vulcan carbon. CO_2R was performed using a custom-made MEA (A = 25 cm^2), where CO_2 gas (Linde, 99.999%) was supplied at 150 sccm through a distilled water humidifier to the cathode chamber. The electrochemical measurements were conducted using a potentiostat (Autolab, PGSTAT302N) equipped with a current booster (10A). For long-term stability testing of the $Cu_{0.98}In_{0.02}$ catalyst, the electrode was prepared by directly loading the catalyst onto the GDL at ~2 mg cm^{-2} without Vulcan carbon, incorporating 2 wt % Nafion perfluorinated resin as a binder, and evaluated in the same custom-made MEA (A = 25 cm^{-2}).

Material characterization

TEM combined with EDX spectroscopy was performed using a JEOL JEM-2200 microscope operated at 200 kV. Powder XRD patterns were collected using a Rigaku MiniFlex 600 diffractometer equipped with monochromatized Cu Kα radiation. XRF analysis was conducted using a Fischerscope X-ray XDAL instrument equipped with a microfocus tungsten (W) X-ray tube operated at 50 kV.

Operando Raman spectroscopy and electrochemical flow-cell study

Operando Raman spectroscopy was performed on a Renishaw inVia Raman microscope equipped with a water-immersion objective and a 785 nm excitation laser. To minimize potential laser-induced damage, spectra were acquired in two separate windows (centered at 700 and 1,700 cm^{-1}). The raw spectra in the 1,700 cm^{-1} range were baseline-corrected using OriginPro 2018 software. An open-structured flow cell was employed,

with a saturated Ag/AgCl electrode and a Pt wire serving as the reference and counter electrodes, respectively. Spectra were collected under chronopotentiometric operation at different applied current densities. Electrochemical flow-cell measurements were conducted following a previously reported method[45] using GDL loaded with 0.6 mg cm^{-2} catalyst and 0.4 mg cm^{-2} Vulcan carbon. The electrolyte was a 0.1 M KH_2PO_4 aqueous solution, and all applied potentials were referenced to RHE (−1.5 V_{RHE}). CO_2 or CO (30 sccm) was supplied to the cathode chamber. For experiments using formate as the reactant, 0.04 M potassium formate (HCOOK, Sigma Aldrich) was dissolved in 0.1 M KH_2PO_4 and used as the electrolyte.

RESOURCE AVAILABILITY

Lead contact

Further information and requests for resources should be directed to and will be fulfilled by the lead contact, David Sinton (dave.sinton@utoronto.ca).

Materials availability

This study did not generate new, unique materials.

Data and code availability

All the experimental data generated in this work and the data used for model training are available on the Zenodo repository dataset for accelerated discovery of multi-element CO_2 electrocatalysts with human-in-the-loop (https://doi.org/10.5281/zenodo.15107045). The Python codes used for ML training and analysis are publicly available on GitHub (https://github.com/jiheonkim10/CO2_to_C3).

ACKNOWLEDGMENTS

This work was supported by the National Research Foundation of Korea (NRF) grant funded by the Korea Government (Ministry of Science and ICT, RS-2023-00250299). The authors acknowledge support from the Alliance for AI-Accelerated Materials Discovery (A3MD). We also acknowledge the support of the Government of Canada's New Frontiers in Research Fund (NFRF), CANSTOREnergy project NFRFT-2022-00197, as well as partial financial support from the University of Toronto's Acceleration Consortium through the Canada First Research Excellence Fund (CFREF-2022-00042) and from the Materials for Clean Fuel (MCF) Challenge program at National Research Council of Canada (NRC).

AUTHOR CONTRIBUTIONS

D.S., E.H.S., and J.H.-S. supervised the project. J.K. conceived the idea, established an accelerated experimental workflow, and performed ML studies. S.M. conceived the data aggregation idea and conducted ML studies with the help of K.L. H.S.L. supported accelerated CO_2R evaluation. Y.B. and Y.L. assisted with Chemspeed operation. R.D., X.L., and C.W. performed *operando* Raman spectroscopy. M.I. conducted TEM characterization. D.K., S.P., A.S.Z., H.S.M., and F.A. contributed to data analysis and interpretation. S.L., Y.C.X., R.K.M., and S.H. contributed to discussions. B.W. assisted with adsorption energy data mining using the AdsorbML pipeline. All authors discussed the results and contributed to manuscript preparation.

DECLARATION OF INTERESTS

The authors declare no competing interests.

SUPPLEMENTAL INFORMATION

Supplemental information can be found online at https://doi.org/10.1016/j.joule.2025.102213.

Received: May 25, 2025
Revised: August 1, 2025
Accepted: October 22, 2025

REFERENCES

1. De Luna, P., Hahn, C., Higgins, D., Jaffer, S.A., Jaramillo, T.F., and Sargent, E.H. (2019). What would it take for renewably powered electrosynthesis to displace petrochemical processes? Science *364*, eaav3506. https://doi.org/10.1126/science.aav3506.
2. O'Brien, C.P., Miao, R.K., Zeraati, A.S., Lee, G.H., Sargent, E.H., and Sinton, D. (2024). CO_2 Electrolyzers. Chem. Rev. *124*, 3648–3693. https://doi.org/10.1021/acs.chemrev.3c00206.
3. Chen, Y.J., Li, X.Y., Chen, Z., Ozden, A., Huang, J.E., Ou, P.F., Dong, J.C., Zhang, J.Q., Tian, C., Lee, B.H., et al. (2024). Efficient multicarbon formation in acidic CO_2 reduction via tandem electrocatalysis. Nat. Nanotechnol. *19*, 311–318. https://doi.org/10.1038/s41565-023-01543-8.
4. Wang, X., Ou, P.F., Ozden, A., Hung, S.F., Tam, J., Gabardo, C.M., Howe, J.Y., Sisler, J., Bertens, K., de Arquer, F.P.G., et al. (2022). Efficient electrosynthesis of *n*-propanol from carbon monoxide using a Ag-Ru-Cu catalyst. Nat. Energy *7*, 170–176. https://doi.org/10.1038/s41560-021-00967-7.
5. Zhan, C., Dattila, F., Rettenmaier, C., Herzog, A., Herran, M., Wagner, T., Scholten, F., Bergmann, A., López, N., and Cuenya, B.R. (2024). Key intermediates and Cu active sites for CO_2 electroreduction to ethylene and ethanol. Nat. Energy *9*, 1485–1496. https://doi.org/10.1038/s41560-024-01633-4.
6. Sun, M.Z., and Huang, B.L. (2024). Direct Machine Learning Predictions of C_3 Pathways. Adv. Energy Mater. *14*, 2400152. https://doi.org/10.1002/aenm.202400152.
7. Han, L.L., Zhu, S.Y., Rao, Z.Y., Scheu, C., Ponge, D., Ludwig, A., Zhang, H.B., Gutfleisch, O., Hahn, H., Li, Z.M., et al. (2024). Multifunctional high-entropy materials. Nat. Rev. Mater. *9*, 846–865. https://doi.org/10.1038/s41578-024-00720-y.
8. Xing, F.L., Nakaya, Y., Yasumura, S., Shimizu, K., and Furukawa, S. (2022). Ternary platinum-cobalt-indium nanoalloy on ceria as a highly efficient catalyst for the oxidative dehydrogenation of propane using CO_2. Nat. Catal. *5*, 55–65. https://doi.org/10.1038/s41929-021-00730-x.
9. Kim, J., Ko, W., Yoo, J.M., Paidi, V.K., Jang, H.Y., Shepit, M., Lee, J., Chang, H., Lee, H.S., Jo, J., et al. (2022). Structural Insights into Multi-Metal Spinel Oxide Nanoparticles for Boosting Oxygen Reduction Electrocatalysis. Adv. Mater. *34*, e2107868. https://doi.org/10.1002/adma.202107868.
10. Angello, N.H., Rathore, V., Beker, W., Wołos, A., Jira, E.R., Roszak, R., Wu, T.C., Schroeder, C.M., Aspuru-Guzik, A., Grzybowski, B.A., et al. (2022). Closed-loop optimization of general reaction conditions for heteroaryl Suzuki-Miyaura coupling. Science *378*, 399–405. https://doi.org/10.1126/science.adc8743.
11. Burger, B., Maffettone, P.M., Gusev, V.V., Aitchison, C.M., Bai, Y., Wang, X.Y., Li, X.B., Alston, B.M., Li, B.Y., Clowes, R., et al. (2020). A mobile robotic chemist. Nature *583*, 237–241. https://doi.org/10.1038/s41586-020-2442-2.
12. Dai, T.W., Vijayakrishnan, S., Szczypiński, F.T., Ayme, J.F., Simaei, E., Fellowes, T., Clowes, R., Kotopanov, L., Shields, C.E., Zhou, Z.X., et al. (2024). Autonomous mobile robots for exploratory synthetic chemistry. Nature *635*, 890–897. https://doi.org/10.1038/s41586-024-08173-7.
13. Chen, T.L., Pang, Z.Q., He, S.M., Li, Y., Shrestha, S., Little, J.M., Yang, H.C., Chung, T.C., Sun, J.Y., Whitley, H.C., et al. (2024). Machine intelligence-accelerated discovery of all-natural plastic substitutes. Nat. Nanotechnol. *19*, 782–791. https://doi.org/10.1038/s41565-024-01635-z.
14. Jones, R.J.R., Lai, Y., Guevarra, D., Kan, K., Haber, J.A., and Gregoire, J.M. (2024). Accelerated screening of gas diffusion electrodes for carbon

dioxide reduction. Digit. Discov. *3*, 1144–1149. https://doi.org/10.1039/D4DD00061G.

15. Soni, A., Ma, S., Ocean, K., Dettelbach, K., Lin, D., Rupnow, C., Mokhtari, M., Waizenegger, C., Crescenzo, G., and Berlinguette, C. (2024). Accelerated development of gas diffusion electrodes for CO_2 electrolyzers. Preprint at ChemRxiv. https://doi.org/10.26434/chemrxiv-2024-znh0f.
16. Kusne, A.G., Yu, H.S., Wu, C.M., Zhang, H.R., Hattrick-Simpers, J., DeCost, B., Sarker, S., Oses, C., Toher, C., Curtarolo, S., et al. (2020). On-the-fly closed-loop materials discovery via Bayesian active learning. Nat. Commun. *11*, 5966. https://doi.org/10.1038/s41467-020-19597-w.
17. Cissé, A., Evangelopoulos, X., Carruthers, S., Gusev, V.V., and Cooper, A.I. (2024). HypBO: Accelerating Black-Box Scientific Experiments Using Experts' Hypotheses. Preprint at arXiv. https://doi.org/10.48550/arXiv.42308.11787.
18. Scheurer, C., and Reuter, K. (2025). Role of the human-in-the-loop in emerging self-driving laboratories for heterogeneous catalysis. Nat. Catal. *8*, 13–19. https://doi.org/10.1038/s41929-024-01275-5.
19. Yao, Z.P., Lum, Y.W., Johnston, A., Mejia-Mendoza, L.M., Zhou, X., Wen, Y.G., Aspuru-Guzik, A., Sargent, E.H., and Seh, Z.W. (2023). Machine learning for a sustainable energy future. Nat. Rev. Mater. *8*, 202–215. https://doi.org/10.1038/s41578-022-00490-5.
20. Chen, J.M., Qiu, H.R., Zhao, Y.L., Yang, H.Z., Fan, L., Liu, Z.H., Xi, S.B., Zheng, G.T., Chen, J.Y., Chen, L., et al. (2024). Selective and stable CO_2 electroreduction at high rates via control of local H_2O/CO_2 ratio. Nat. Commun. *15*, 5893. https://doi.org/10.1038/s41467-024-50269-1.
21. Gong, Q.F., Ding, P., Xu, M.Q., Zhu, X.R., Wang, M.Y., Deng, J., Ma, Q., Han, N., Zhu, Y., Lu, J., et al. (2019). Structural defects on converted bismuth oxide nanotubes enable highly active electrocatalysis of carbon dioxide reduction. Nat. Commun. *10*, 2807. https://doi.org/10.1038/s41467-019-10819-4.
22. Gabardo, C.M., O'Brien, C.P., Edwards, J.P., McCallum, C., Xu, Y., Dinh, C.T., Li, J., Sargent, E.H., and Sinton, D. (2019). Continuous Carbon Dioxide Electroreduction to Concentrated Multi-carbon Products Using a Membrane Electrode Assembly. Joule *3*, 2777–2791. https://doi.org/10.1016/j.joule.2019.07.021.
23. Kose, T., O'Brien, C.P., Wicks, J., Abed, J., Xiao, Y.C., Sutherland, B., Sarkar, A., Jaffer, S.A., Sargent, E.H., and Sinton, D. (2022). High-throughput parallelized testing of membrane electrode assemblies for CO_2 reduction. Catal. Sci. Technol. *12*, 6239–6245. https://doi.org/10.1039/D2CY00873D.
24. Kortlever, R., Shen, J., Schouten, K.J.P., Calle-Vallejo, F., and Koper, M.T.M. (2015). Catalysts and Reaction Pathways for the Electrochemical Reduction of Carbon Dioxide. J. Phys. Chem. Lett. *6*, 4073–4082. https://doi.org/10.1021/acs.jpclett.5b01559.
25. Feaster, J.T., Shi, C., Cave, E.R., Hatsukade, T.T., Abram, D.N., Kuhl, K.P., Hahn, C., Nørskov, J.K., and Jaramillo, T.F. (2017). Understanding Selectivity for the Electrochemical Reduction of Carbon Dioxide to Formic Acid and Carbon Monoxide on Metal Electrodes. ACS Catal. *7*, 4822–4827. https://doi.org/10.1021/acscatal.7b00687.
26. Todorova, T.K., Schreiber, M.W., and Fontecave, M. (2020). Mechanistic Understanding of CO_2 Reduction Reaction (CO2RR) Toward Multicarbon Products by Heterogeneous Copper-Based Catalysts. ACS Catal. *10*, 1754–1768. https://doi.org/10.1021/acscatal.9b04746.
27. Nitopi, S., Bertheussen, E., Scott, S.B., Liu, X.Y., Engstfeld, A.K., Horch, S., Seger, B., Stephens, I.E.L., Chan, K., Hahn, C., et al. (2019). Progress and Perspectives of Electrochemical CO_2 Reduction on Copper in Aqueous Electrolyte. Chem. Rev. *119*, 7610–7672. https://doi.org/10.1021/acs.chemrev.8b00705.
28. Peterson, A.A., and Nørskov, J.K. (2012). Activity Descriptors for CO_2 Electroreduction to Methane on Transition-Metal Catalysts. J. Phys. Chem. Lett. *3*, 251–258. https://doi.org/10.1021/jz201461p.
29. Schrier, J., Norquist, A.J., Buonassisi, T., and Brgoch, J. (2023). In Pursuit of the Exceptional: Research Directions for Machine Learning in Chemical and Materials Science. J. Am. Chem. Soc. *145*, 21699–21716. https://doi.org/10.1021/jacs.3c04783.
30. Nori, N., Jenkins, S., Koch, P., and Caruana, R. (2019). InterpretML: A unified framework for machine learning interpretability. Preprint at arXiv. https://doi.org/10.48550/arXiv.1909.09223.
31. Esterhuizen, J.A., Goldsmith, B.R., and Linic, S. (2022). Interpretable machine learning for knowledge generation in heterogeneous catalysis. Nat. Catal. *5*, 175–184. https://doi.org/10.1038/s41929-022-00744-z.
32. Hastie, T.J. (2017). Ch. 7 Statistical Models in S, J.M. Chambers and T.J. Hastie, eds. (Routledge), pp. 249–307. https://doi.org/10.1201/9780203738535-7.
33. Hastie, T., Tibshirani, R., and Friedman, J.H. (2009). Ch. 2.9 The Elements of Statistical Learning: Data Mining, Inference, and Prediction (Springer).
34. Shalev-Shwartz, S., and Ben-David, S. (2014). Ch. 5 Understanding Machine Learning: from Foundations to Algorithms (Cambridge University Press).
35. Lan, J., Palizhati, A., Shuaibi, M., Wood, B.M., Wander, B., Das, A., Uyttendaele, M., Zitnick, C.L., and Ulissi, Z.W. (2023). AdsorbML: a leap in efficiency for adsorption energy calculations using generalizable machine learning potentials. Npj Comput. Mater. *9*, 172. https://doi.org/10.1038/s41524-023-01121-5.
36. Abed, J., Kim, J., Shuaibi, M., Wander, B., Duijf, B., Mahesh, S., Lee, H.S., V., G., Hoogland, S., et al. (2024). Open Catalyst Experiments 2024, (OCx24): Bridging Experiments and Computational Models. Preprint at arXiv. https://doi.org/10.48550/arXiv.2411.11783.
37. Wang, Z.J., Kale, A., H., N., P., S., E., N., H., C.D., et al. (2022). Interpretability, then what? Editing machine learning models to reflect human knowledge and values. Preprint at arXiv. https://doi.org/10.1145/3534678.3539074.
38. Gao, J., Bahmanpour, A., Kröcher, O., Zakeeruddin, S.M., Ren, D., and Grätzel, M. (2023). Electrochemical synthesis of propylene from carbon dioxide on copper nanocrystals. Nat. Chem. *15*, 705–713. https://doi.org/10.1038/s41557-023-01163-8.
39. Patel, A.M., Nørskov, J.K., Persson, K.A., and Montoya, J.H. (2019). Efficient Pourbaix diagrams of many-element compounds. Phys. Chem. Chem. Phys. *21*, 25323–25327. https://doi.org/10.1039/c9cp04799a.
40. de Smit, E., and Weckhuysen, B.M. (2008). The renaissance of iron-based Fischer-Tropsch synthesis: on the multifaceted catalyst deactivation behaviour. Chem. Soc. Rev. *37*, 2758–2781. https://doi.org/10.1039/b805427d.
41. Ellis, P.R., Enache, D.I., James, D.W., Jones, D.S., and Kelly, G.J. (2019). A robust and precious metal-free high performance cobalt Fischer-Tropsch catalyst. Nat. Catal. *2*, 623–631. https://doi.org/10.1038/s41929-019-0288-5.
42. Cheng, Q.P., Tian, Y., Lyu, S.S., Zhao, N., Ma, K., Ding, T., Jiang, Z., Wang, L.H., Zhang, J., Zheng, L.R., et al. (2018). Confined small-sized cobalt catalysts stimulate carbon-chain growth reversely by modifying ASF law of Fischer-Tropsch synthesis. Nat. Commun. *9*, 3250. https://doi.org/10.1038/s41467-018-05755-8.
43. Chen, H., Lian, Z., Zhao, X., Wan, J.W., Pieters, P.F., Oliver-Meseguer, J., Yang, J., Pach, E., Carenco, S., Treps, L., et al. (2024). The role of manganese in CoMnO catalysts for selective long-chain hydrocarbon production via Fischer-Tropsch synthesis. Nat. Commun. *15*, 10294. https://doi.org/10.1038/s41467-024-54578-3.
44. Montoya, J.H., Shi, C., Chan, K., and Nørskov, J.K. (2015). Theoretical Insights into a CO Dimerization Mechanism in CO_2 Electroreduction. J. Phys. Chem. Lett. *6*, 2032–2037. https://doi.org/10.1021/acs.jpclett.5b00722.
45. Zhou, Y.S., Martín, A.J., Dattila, F., Xi, S.B., López, N., Pérez-Ramírez, J., and Yeo, B.S. (2022). Long-chain hydrocarbons by CO_2 electroreduction using polarized nickel catalysts. Nat. Catal. *5*, 545–554. https://doi.org/10.1038/s41929-022-00803-5.

46. Gao, J., Zhang, H., Guo, X.Y., Luo, J.S., Zakeeruddin, S.M., Ren, D., and Grätzel, M. (2019). Selective C–C Coupling in Carbon Dioxide Electroreduction via Efficient Spillover of Intermediates As Supported by Operando Raman Spectroscopy. J. Am. Chem. Soc. *141*, 18704–18714. https://doi.org/10.1021/jacs.9b07415.

47. Ren, D., Gao, J., Zakeeruddin, S.M., and Grätzel, M. (2021). New Insights into the Interface of Electrochemical Flow Cells for Carbon Dioxide Reduction to Ethylene. J. Phys. Chem. Lett. *12*, 7583–7589. https://doi.org/10.1021/acs.jpclett.1c02043.

48. Zhan, C., Dattila, F., Rettenmaier, C., Bergmann, A., Kühl, S., García-Muelas, R., López, N., and Cuenya, B.R. (2021). Revealing the CO Coverage-Driven C–C Coupling Mechanism for Electrochemical CO_2 Reduction on Cu_2O Nanocubes *via* Raman Spectroscopy. ACS Catal. *11*, 7694–7701. https://doi.org/10.1021/acscatal.1c01478.

49. Chou, T.C., Chang, C.C., Yu, H.L., Yu, W.Y., Dong, C.L., Velasco-Vélez, J.J., Chuang, C.H., Chen, L.C., Lee, J.F., Chen, J.M., et al. (2020). Controlling the Oxidation State of the Cu Electrode and Reaction Intermediates for Electrochemical CO_2 Reduction to Ethylene. J. Am. Chem. Soc. *142*, 2857–2867. https://doi.org/10.1021/jacs.9b11126.

50. Dorakhan, R., Grigioni, I., Lee, B.H., Ou, P.F., Abed, J., O'Brien, C., Rasouli, A.S., Plodinec, M., Miao, R.K., Shirzadi, E., et al. (2023). A silver-copper oxide catalyst for acetate electrosynthesis from carbon monoxide. Nat. Synth. *2*, 448–457. https://doi.org/10.1038/s44160-023-00259-w.

51. Chernyshova, I.V., Somasundaran, P., and Ponnurangam, S. (2018). On the origin of the elusive first intermediate of CO_2 electroreduction. Proc. Natl. Acad. Sci. USA *115*, E9261–E9270. https://doi.org/10.1073/pnas.1802256115.

52. Kim, Y., Park, S., Shin, S.J., Choi, W., Min, B.K., Kim, H., Kim, W., and Hwang, Y.J. (2020). Time-resolved observation of C-C coupling intermediates on Cu electrodes for selective electrochemical CO_2 reduction. Energy Environ. Sci. *13*, 4301–4311. https://doi.org/10.1039/D0EE01690J.

53. Li, F.W., Thevenon, A., Rosas-Hernández, A., Wang, Z.Y., Li, Y.L., Gabardo, C.M., Ozden, A., Dinh, C.T., Li, J., Wang, Y.H., et al. (2020). Molecular tuning of CO_2-to-ethylene conversion. Nature *577*, 509–513. https://doi.org/10.1038/s41586-019-1782-2.

54. Yoo, S., Park, S., Son, J., Kim, J., Shin, H., and Hwang, Y.J. (2025). Excess Cations Alter *CO Intermediate Configuration and Product Selectivity of Cu in Acidic Electrochemical CO_2 Reduction Reaction. J. Am. Chem. Soc. *147*, 12996–13007. https://doi.org/10.1021/jacs.5c02954.

55. Liao, Y.-L., Wood, B., Das, A., and Smidt, T. (2023). EquiformerV2: improved Equivariant transformer for scaling to higher-degree representations. Preprint at arXiv. https://doi.org/10.48550/arXiv.2306.12059.